Lab on a Chip

A human initial lymphatic chip reveals distinct mechanisms of primary lymphatic valve dysfunction in acute and chronic inflammation

Journal:	*Lab on a Chip*
Manuscript ID	LC-ART-06-2023-000486.R1
Article Type:	Paper
Date Submitted by the Author:	21-Sep-2023
Complete List of Authors:	Kraus, Samantha; Cornell University, Nancy E. and Peter C. Meinig School of Biomedical Engineering Lee, Esak; Cornell University, Nancy E. and Peter C. Meinig School of Biomedical Engineering

ARTICLE

A human initial lymphatic chip reveals distinct mechanisms of primary lymphatic valve dysfunction in acute and chronic inflammation

Received 00th January 20xx,
Accepted 00th January 20xx

DOI: 10.1039/x0xx00000x

Samantha Kraus[a] and Esak Lee [a, *]

Interstitial fluid uptake and retention by lymphatic vessels (LVs) play a role in maintaining interstitial fluid homeostasis. While it is well-established that intraluminal lymphatic valves in the collecting LVs prevent fluid backflow (secondary lymphatic valves), a separate valve system in the initial LVs that only permits interstitial fluid influx into the LVs, preventing fluid leakage back to the interstitium (primary lymphatic valves), remains incompletely understood. Although lymphatic dysfunction is commonly observed in inflammation and autoimmune diseases, how the primary lymphatic valves are affected by acute and chronic inflammation has scarcely been explored and even less so using *in vitro* lymphatic models. Here, we developed a human initial lymphatic vessel chip where interstitial fluid pressure and luminal fluid pressure are controlled to examine primary lymph valve function. In normal conditions, lymphatic drainage (fluid uptake) and permeability (fluid leakage) in engineered LVs were maintained high and low, respectively, which was consistent with our understanding of healthy primary lymph valves. Next, we examined the effects of acute and chronic inflammation. Under the acute inflammation condition with a TNF-α treatment (2 hours), degradation of fibrillin and impeded lymphatic drainage were observed, which were reversed by treatment with anti-inflammatory dexamethasone. Surprisingly, the chronic inflammation condition (repeated TNF-α treatments during 48 hours) deposited fibrillin to compensate for the fibrillin loss, showing no change in lymphatic drainage. Instead, the chronic inflammation condition led to cell death and disruption of lymphatic endothelial cell-cell junctions, increasing lymphatic permeability and fluid leakage. Our human lymphatic model shows two distinct mechanisms by which primary lymphatic valve dysfunction occurs in acute and chronic inflammation.

Introduction

The lymphatic system is integral for the recirculation of fluid and cells throughout the body to maintain interstitial fluid and tissue homeostasis as well as provide routes for the trafficking of antigen-presenting cells and lymphocytes to lymph nodes for the adaptive immune response.[1] Interstitial fluid uptake from the surrounding tissue by the lymphatics generally occurs by hydrostatic and colloidal osmotic pressure gradients, which allow fluid entry into the lymphatic capillaries, or initial lymphatic vessels (LVs). The initial LVs are composed of a single layer of lymphatic endothelial cells (LECs) with a discontinuous basement membrane and specialized "button-like" cell-cell junctions that are highly permeable to solutes and molecules inflow, but prevent backflow to the interstitium.[2] The initial LVs converge into the collecting LVs, which are less permeable due to the presence of "zipper-like" cell-cell junctions. The collecting LVs are covered with perivascular layers of lymphatic muscle cells (LMCs), which possess characteristics of both smooth muscle cells and cardiac striated muscle cells to endow them with the capability of modulating vascular tone and rhythmic contraction.[3-6] Moreover, the collecting LVs prevent luminal fluid backflow with intraluminal lymphatic valves (or "secondary" lymphatic valves).[7-9]

While the "secondary" lymphatic valves in the collecting LVs have been extensively studied,[7, 8, 10, 11] it is poorly understood how the initial LVs enable unidirectional interstitial fluid uptake and retention. One of the most promising explanations for this phenomenon is the existence of a "primary" lymphatic valve system in the initial lymphatic capillaries, in which free overlapping cell edges anchored on each side by the unique button-like junctions form "flap valves" that allow fluid to flow unidirectionally along its pressure gradient into the capillary lumen **(Fig. 1A)**.[12] One of the first studies showing evidence for this system demonstrated the pressure gradient-dependent transport of fluorescent nanospheres across initial LVs in mice using micropipette manipulation, in which high interstitial fluid pressure promotes entry of lymph fluid and cells into the lumen.[13, 14] Integral to the primary lymphatic valve model is the presence of fibrillin-rich anchoring filaments that connect the lymphatic endothelium to the surrounding tissue and extracellular matrix (ECM).[15] Mathematical and computational models also suggest that low interstitial fluid pressure (or high luminal fluid pressure) places the primary valves in an

[a] *Nancy E. and Peter C. Meinig School of Biomedical Engineering, Cornell University, Ithaca, NY 14853, USA*
[*] *Correspondence: Esak Lee, Nancy E. and Peter C. Meinig School of Biomedical Engineering, Cornell University, 302 Weill Hall, 237 Tower Rd, Ithaca, NY 14853, USA. Email: el767@cornell.edu*
Electronic Supplementary Information (ESI) available: [details of any supplementary information available should be included here]. See DOI: 10.1039/x0xx00000x

impermeable state tethered to the surrounding tissue preventing fluid leakage, while increased interstitial fluid pressure (or decreased luminal fluid pressure) allows the tensioned anchoring filaments to pull apart the overlapping junctions and allow interstitial fluid and cells to flow into the LV lumen without causing a collapse of the lymph vessels.[16, 17] In fact, increased lymphatic leakage, impaired drainage, and lymphedema have been associated with mice knockout models of Emilin1, an elastic microfibril-associated protein also involved in anchoring filaments.[18, 19]

Lymphatic dysfunction is often observed in inflammatory and autoimmune diseases.[20, 21] However, very few studies have examined the specific effects of physiological inflammation, both acute and chronic, on primary lymphatic valves, which is of particular interest given the substantial role of initial lymphatics in inflammatory disease.[22] For instance, a recent study demonstrated that inflammation via tumor necrosis factor-alpha (TNF-α), which occurs in the autoimmune Crohn's disease of the small intestines, causes the formation of tertiary lymphoid organs and impaired mesenteric lymphatic function in mice models. Further, adding TNF-α to *in vitro* culture of lymphatic endothelial cells (LECs) downregulated collecting valve-associated genes, showing the extent to which inflammatory signaling compromises secondary lymph valve integrity in the collecting LVs.[23] As to what occurs in the primary lymph valves in the initial LVs, induction of inflammation via platelet-activating factors in mice models has been shown to impair fluid clearance and vessel permeability.[24] There have been also studies to suggest that button junctions in initial LVs become "zippered" in inflammation[22] and VEGF-A signaling.[25] To our best knowledge, the effect of inflammatory conditions on primary lymphatic valve function has not yet been studied *in vitro* using three-dimensional (3D) microfluidic platforms, which is beneficial for patient-specific testing, drug screening, and the discovery of fundamental behaviors of the initial LVs.

To address this challenge, we created a human lymphatic vessel (LV) chip where interstitial fluid pressure and luminal fluid pressure can be tuned to test primary lymph valve function and discovered two distinct mechanisms by which primary lymphatic valve dysfunction occurs in acute and chronic inflammation. The acute inflammation condition led to the degradation of fibrillin and impeded lymphatic drainage. However, the chronic inflammation condition expressed and deposited fibrillin to compensate for the fibrillin loss with no change in lymphatic drainage. Despite the fibrillin deposition, the chronic inflammation condition still showed lymphatic dysfunction by leading to a disruption of lymphatic endothelial cell-cell junctions and increasing lymphatic permeability and leakage.

Experimental

Cell Culture

Primary human dermal lymphatic endothelial cells (LECs), isolated from dermal tissues of neonatal donors, were kindly gifted from Dr. Young Kwon Hong (University of Southern California). These cells have been characterized using several lymphatic endothelial markers in Dr. Hong's lab.[26, 27] For additional characterization of lymphatic phenotype, engineered LEC vessels showed no statistically significant difference in the number of DAPI+ and Prox1+ stained nuclei for every image in each group (control, acute inflammation, and chronic inflammation), indicating there was significant colocalization between DAPI and Prox1 for all groups **(Supplementary Fig. 1)**. LECs were cultured in EGM-2MV media (Lonza, Switzerland), used in their passages 6-12 and maintained in standard tissue culture incubators at 37°C, 95% humidity, and 5% CO_2.

Microfluidics

Microfluidic devices were fabricated using a soft lithography method as we performed previously.[28-31] Briefly, the human lymphatic vessel (LV) chip was composed of a polydimethylsiloxane (PDMS) housing for two channels. The PDMS (Sylgard 184, Dow-Corning, Midland, MI) was formed by mixing with a curing agent from the Sylgard PDMS kit at a 10:1 ratio of base to curing agent and poured into silicon master molds for overnight curing at 80°C. After removal from the molds, the PDMS was treated with plasma etching and attached to a cover glass. The devices were then treated with 0.01% poly-L-lysine (Sigma, St Louis, MO) for 1 hour and 1% glutaraldehyde for 30 minutes, then rinsed thoroughly overnight. The channels of the device were prepared by inserting steel acupuncture needles of 0.25 mm diameter, sterilized, and coated with bovine serum albumin (BSA). Rat tail Collagen 1 hydrogel (Corning, at final collagen concentration: 2.5 mg/ml) was pipetted into the devices to form a cohesive extracellular matrix and polymerized for 50 minutes at 37°C. For our purposes, the collagen 1 ECM was chosen for support of LEC growth as used in past studies from our lab[31] and based on behavior *in vivo*.[32] Similar studies have found that a 2.5 mg/mL collagen 1 hydrogel is characterized by a G' of 62.14 ± 4.87 Pa and supports vascular tube formation as well as lymphatic extracellular matrix.[33-35] Ensuing overnight media washing and needle removal, LECs were added to one of the two channels by resuspending the cells at 1.25×10^6 cells/mL in LEC media and introducing the cell solution to a single channel to allow cell adhesion to the 3D collagen matrix for 10 minutes before washing out excess cells with growth medium. The devices were incubated for 1-2 days on a rocking platform in the tissue culture incubator, replenishing culture media daily **(Figs. 1B-D)**. For determining the shear stress imparted by a rocker, we assumed that the culture medium is a Newtonian fluid in which the viscous stresses arising from its flow, at every point, are linearly correlated to the local strain rate, as detailed in our previous study.[31] We determined that the shear stress created by the rocker, 3.5 ~ 4.5 dyne/cm^2 falls within the physiological range of 4 ~ 12 dyne/cm^2 seen in rat mesenteric pre-nodal lymphatics.[36]

Inflammation Models

The lymphatic chips after growth for 1-2 days to form engineered LVs were treated with 10 or 20 ng/mL of Recombinant Human TNF-α (PeproTech, Cranbury, NJ) in EGM-

2MV media. In terms of the exposure time, 2 hours was chosen to represent acute inflammation as a measure of cytokine exposure on the order of hours, and 48 hours was chosen to represent chronic inflammation as a measure of cytokine exposure on the order of days, which has been done previously with LECs *in vitro*.[23, 37] To model acute inflammation, the devices were treated with TNF-α (10 or 20 ng/mL) for 2 hours and the primary lymphatic valve function (lymphatic drainage and lymphatic permeability) was assessed. To model chronic inflammation, we had a 48-hour span: for the 48-hour treatment, we treated the devices with TNF-α (10 or 20 ng/mL), let them incubate for 24 hours, then treated them again with fresh TNF-α in the daily media change for another 24 hours before testing the primary lymphatic valve function. To verify the effect of these TNF-α inflammation models on LEC viability, the LECs were seeded in 2D, 6-well plate and 3D microfluidic chip vessel culture and treated with either 2 hours or 48 hours of TNF-α or control conditions, then stained with a LIVE/DEAD™ Cell Imaging Kit (488/570) (Invitrogen, Waltham, MA) for quantification of the ratio of live/dead cells.

Anti-inflammatory Treatment

To determine if the decreased vessel drainage under acute inflammation and increased vessel permeability under chronic inflammation could be reversed by anti-inflammatory drug treatment, the lymphatic chips, one day prior to exposure to 10 or 20 ng/mL of Recombinant Human TNF-α as described previously for the acute and chronic time periods, were pre-treated with 1 μM of anti-inflammatory dexamethasone (Sigma, St. Louis, MO) in EGM-2MV media. Thereafter, dexamethasone treatment was continued in conjunction with 2 hr or 48 hr TNF-α inflammation. Drainage and permeability assays were then conducted as described for pre-treated acute and chronically inflamed chips, respectively, along with immunostaining and imaging.

Lymphatic Drainage

For measuring lymphatic drainage (fluid uptake) in the microfluidic chip devices, fluorescent Dragon Green nanospheres (Bangs Laboratories, Fishers, IN) were mixed into the EGM-2MV media solution at a dilution of 1:1000 and added to the reservoirs on the opposite side of the lymphatic vascular channel to establish an interstitial fluid pressure gradient across the collagen 1 hydrogel toward the lymphatic vessel **(Fig. 1E)**. The nanospheres were confirmed to have a 66.63 ± 4.007 nm diameter (PDI = 0.023) by dynamic light scattering on a Malvern Nano ZS Zetasizer **(Fig. 2A)**. For evaluation of proper lymphatic primary valve function in the control condition, the lack of a fluid pressure gradient was established by introducing media to both sides of the chip **(Fig. 2B-C)**. Fluorescent nanospheres were chosen for the drainage studies to represent larger macromolecules and proteins, and also due to the fact that the landmark studies showing primary valve function *in vivo* utilized fluorescent nanospheres of similar size, which helps to correlate our findings with *in vivo* work.[13, 14] After allowing the fluid flow to reach equilibrium after 16 hours, the media was collected from reservoirs on both the vascular and avascular sides, and the samples were weighed to find the fluid volume collected given the known density of the nanoparticle solution. The concentration of nanoparticles in the collected samples was then found by fluorescence spectroscopy using a SpectraMax M2 Microplate Reader (Molecular Devices, San Jose, CA) and SoftMax® Pro 7 Software with a standard curve of known concentrations in media. The degree of nanoparticle drainage was then determined as the percentage of total nanoparticles loaded that were drained to the lymphatic vascular channel.

Lymphatic Permeability

Lymphatic permeability (fluid leakage) in microfluidic devices was measured using 70 kDa dextran as described previously.[28, 29, 38] 70 kDa dextran was chosen to represent albumin, electrolytes, and immunoglobulins that are transported through the lymphatics and most susceptible to leakage from the initial lymphatic vessels, and has been used extensively in previous studies characterizing LEC permeability. Briefly, fluorescently labeled dextran (70 kDa, FITC, Life Technologies, Carlsbad, CA) was mixed in the media solution (dextran concentration in the solution: 25 μg/mL) and 50 μL of the dextran solution was added to one reservoir that is connected to the other reservoir through the lymphatic vascular channel **(Fig. 1F)**. This initial hydrostatic pressure allows fluid to fill the vessel lumen. We imaged the vessel area (in a 10x field) that is sufficiently far from the dextran injection to minimize data fluctuation due to the initial loading pressure. We imaged dextran diffusion to collagen matrix for 5 minutes after injection every 5 seconds with an SP8 confocal microscope (Leica, Germany). We adopted the automized MATLAB code developed previously, which in summary determines a linear fit for the integrated density of fluorescence signal in the interstitium (gel) over time and takes the slope of that fit as the diffusive permeability in cm/s, to quantify permeability from time-lapse images **(Supplementary Fig. 2)**.[28, 29, 38]

Immunostaining and Imaging in Microfluidics

For immunofluorescent staining and imaging, LEC-generated engineered lymphatic vessels (LVs) embedded in the 3D collagen 1 matrix of the device were fixed with 4% paraformaldehyde (Electron Microscopy Sciences, Hatfield, PA). Fixed devices were permeated with PBST (0.3% Triton-X in PBS), then blocked with 3% BSA in PBS overnight at 4°C. Primary antibodies detecting fibrillin (Millipore Sigma, 1:300, clone 11C1.3) were incubated in a blocking buffer overnight at 4°C and then washed with PBS. Secondary antibodies (all from Invitrogen, Waltham, MA, 1:500), Phalloidin (Life Technologies, 1:200), and DAPI (Sigma, 1:500) were subsequently incubated in a blocking buffer overnight at 4°C in the dark and washed with PBS once more. Confocal images were acquired with an SP8 confocal microscope (Leica) with a 40× objective. Obtained fluorescent images were z-stacked and adjusted for brightness and contrast using ImageJ.[39, 40] Equal-size images of vessels from all treatments and exposure times were thresholded to find the signal intensity normalized to cell number and area of

the fibrillin signal as a fraction of the whole vessel area using ImageJ. In order to examine the degree of junction disruption between LECs in lymph vessels treated under different inflammatory conditions, the aforementioned fixing, staining, and imaging procedures were used, with the primary antibodies changed to detect VE-cadherin (Santa Cruz Biotechnology, Dallas, TX, 1:100) and Prox1 (ReliaTech GmbH, Germany, 1:100). Equal size images of vessels from all treatment conditions were obtained and cell borders (30 cells for each image) were identified manually using ImageJ.[39] The line intensity profile across the cell border was plotted for each cell to define values below a selected threshold as discontinuities to be counted, measuring the degree of gaps between cells. Quantification of the percentage vessel gap area and the relative junctional area occupied by VE-cadherin staining was found similarly by thresholding to calculate blank space as a fraction of the whole vessel area and VE-cadherin signal as a fraction of the whole vessel area, respectively.

Statistics

Independent two-sample populations were compared using unpaired, two-sample t-tests with a normal distribution assumption. For group analyses, one-way ANOVAs with Tukey's HSD (Honestly Significant Difference) tests were used to compare the mean values. All P values were two-sided, and *P < 0.05 were considered statistically significant. Statistical analyses were performed using GraphPad Prism 9. All data points on the graphs represent average values, and error bars depict the Standard Error of the Mean (SEM).

Results and discussion

An engineered 3D lymphatic model to examine primary lymphatic valve function

To examine primary lymphatic valve function, we aimed to determine lymphatic drainage (fluid uptake) and permeability (fluid leakage) in normal and inflammation conditions. To achieve this, we engineered an organotypic model of LVs.[30, 31] Briefly, our PDMS (polydimethylsiloxane)-based LV-on-chip is composed of two hollow cylindrical channels, which are completely embedded into a 3D collagen 1 matrix **(Fig. 1B)**. In one of the hollow channels, we seeded human dermal lymphatic endothelial cells (LECs) to form an engineered LV (a LEC channel on the right side in **Fig. 1B**). The EGM-2MV media was introduced to circular reservoirs (inlet and outlet) that are directly connected to the lymphatic endothelial channel. A luminal shear flow of 3.5-4.5 dyne/cm^2 was initiated to culture the LECs by rocking the lymphatic vessel-on-chip device in a tissue culture incubator. After a couple of days of culturing LECs on the rocking platform, LECs were stabilized in the channel, forming a rudimentary engineered LV **(Fig. 1C)**. To test the lymphatic identity and the structure of the LVs, LECs in the device were stained with anti-Prox1 antibodies, anti-VE-cadherin antibodies, and DAPI. Prox1 is a lymphatic endothelial-specific transcription factor residing in the cell nucleus, and VE-cadherin is an adherens junction marker in endothelial cells **(Fig. 1D and Supplementary Fig. 1)**.

In the canonical model of primary lymphatic valve function, the "flap valves" open to allow drainage of lymph fluid and molecules under high interstitial fluid pressure (expansion phase), but the flap valves close under high luminal fluid pressure after finishing the initial lymphatic drainage (compression phase) **(Fig. 1A)**. To model the first step, "opening of the flap valves" in lymphatic drainage, we left the remaining channel empty (an acellular channel on the left side in **Figure 1B**) and introduced excess fluid mixed with fluorescently labeled nanospheres to the acellular channel to form high interstitial fluid pressure against the LEC channel for a "drainage assay" **(Fig. 1E)**. The average diameter of the nanospheres used was 66.63 ± 4.007 nm (PDI = 0.023) **(Fig. 2A)**. For evaluation of proper lymphatic primary valve function in the control condition, we prepared two different conditions: fluid pressure gradient condition **(Fig. 2B)** vs. no fluid pressure gradient condition **(Fig. 2C)**. To introduce a "fluid pressure gradient," we added media mixed with nanoparticles into one side of the channels **(Fig. 2B)**. To model the "no fluid pressure gradient" condition, we introduced media to both sides of the channels, and the nanoparticles were only included with the media in the left side channel **(Fig. 2C)**. As expected, drainage was significantly lower (**p = 0.0021) in the absence of the fluid pressure gradient than the condition with fluid pressure gradient, demonstrating that our LEC channel exhibits proper primary valve function by opening under a high interstitial fluid pressure gradient **(Fig. 2D)**. After allowing the fluid flow to reach equilibrium, the media was collected from reservoirs on both the acellular channel and LEC channel sides and the samples were weighed to find the fluid volume collected given the known density of the nanoparticle solution. The degree of nanoparticle drainage was then determined as the percentage of total nanoparticles loaded that were drained to the lymphatic vascular channel **(Fig. 2D)**. To study the "closing of the flap valves" after finishing lymphatic drainage, we left the remaining channel empty and introduced fluid directly to the lumen of the LEC channel to increase luminal fluid pressure for a "permeability assay" **(Fig. 1F)**. Briefly, fluorescently labeled dextran (70 kDa) was mixed in the media solution and the dextran solution was added to one reservoir that is connected to the other reservoir through the LEC channel **(Fig. 1F)**. This initial luminal pressure allows fluid to fill the vessel lumen. We imaged the dextran diffusion out of the LEC channel to assess the retention of the fluid when there is higher luminal fluid pressure. Together, these two experimental settings modeling the "expansion phase" and the "compression phage" show two important steps of the primary valve function: (i) interstitial fluid drainage into a lymphatic vessel **(Fig. 1E)** and (ii) the retention of the drained "lymph" in the lymphatic vessel **(Fig. 1F)**. We examine these primary lymph valve functions in the normal or inflammation condition.

Engineered primary lymphatic valves exhibit decreased drainage under acute inflammation

For evaluation of the lymphatic drainage capacity of the primary lymph valves, conceptually described in **Figure 1E**, fluorescently labeled nanospheres of mean diameter 66.63 ± 4.007 nm **(Fig. 2A)** were mixed in LEC media**,** and the mixed solution was introduced to the reservoirs connected to the acellular channel, on the far side from the LEC channel to introduce interstitial fluid pressure in the system. After 16 hours of introduction of interstitial fluid, the extent of fluid drainage to the LEC channel-associated reservoirs was measured by collecting the drained media and measuring their spectrophotometry. Under acute inflammation (2-hour treatment with TNF-α), drainage capacity decreased by 51.9% compared to untreated control (p = 0.0018) **(Fig. 2E)**. Conversely, drainage capacity of vessels under chronic inflammation (repeated treatments with TNF-α during 48 hours), did not show significant changes in lymphatic drainage capacity **(Fig. 2E)**. Together, these data suggested that engineered lymphatic vessels exhibit impaired drainage (impeded fluid uptake) under acute inflammation condition than in the normal or chronic inflammation condition.

Engineered primary lymphatic valves exhibit increased permeability under chronic inflammation

For evaluation of lymphatic permeability (fluid leakage) of the primary lymph valves, conceptually described in **Figure 1F**, we introduced fluorescently labeled dextran directly into the vessel lumens and observed dextran diffusion to the interstitial space in real time under microscopy **(Fig. 3)**. Under acute inflammation, vessel permeability did not change significantly **(Fig. 3A)**. Conversely, lymphatic permeability dramatically increased under the chronic inflammation condition over the course of days, up to a 2.4-fold increase (p = 0.0319) **(Fig. 3A)**. This is further elucidated by live imaging of lymphatic permeability over the course of 90 seconds **(Fig. 3B)**.

Changes in lymphatic drainage capacity in the acute inflammation condition correlate with alterations in fibrillin expression

It is believed that lymphatic drainage into the initial LVs is mediated by fibrillin-rich anchoring filaments.[15] In order to investigate the putative role of anchoring filaments in the changes of lymphatic drainage associated with TNF-α induced inflammation, confocal fluorescence images were taken of the fixed lymphatic vessels stained with anti-fibrillin antibodies, phalloidin, and DAPI **(Figs. 4A-C)**. From the visual analysis of these images, it appears that TNF-α treated vessels differ from controls in terms of the organization and density of fibrillin, an integral component of the anchoring filaments that pull apart the primary valves of the initial lymphatics. Fibrillin expression was quantified with image analysis to find the area that the fibrillin filaments occupy as a fraction of the whole vessel area **(Fig. 4D)**. In regard to the area fraction of fibrillin over the whole vessel, acute inflammation appears to decrease fibrillin area fraction by 35.5%, with the decrease fibrillin density under acute inflammation being statistically significant compared to control (p = 0.0349) **(Fig. 4D)**. As fibrillin fluorescence area fraction in immunostaining is proportional to fibrillin content within the LECs, fibrillin degradation appears to occur under acute inflammation. However, chronic inflammation expressed and deposited fibrillin and compensated for the fibrillin loss in the acute condition, as shown in the non-significant difference in fibrillin area fraction in the chronic inflammation condition and normal condition **(Fig. 4D)**. Taken together, the acute inflammation condition leads to the degradation of fibrillin **(Fig. 4D)** and impedes lymphatic drainage **(Fig. 2E)**. However, the chronic inflammation condition expresses and deposits fibrillin to compensate for the fibrillin loss, showing no change in lymphatic drainage.

Changes in lymphatic permeability in the chronic inflammation condition correlate with alterations in lymphatic endothelial cell-cell junctions

As anchoring filaments (fibrillin) of the primary lymphatic valves act to mediate interstitial fluid uptake, fluid retention is regulated by the lymphatic permeability of adherens junctions in the lymphatic endothelium under the compression phase. To examine the roles of inflammation in the lymphatic endothelial adherens junctions and permeability, we examined the effect of TNF-α induced inflammation (acute vs. chronic) on the paracellular adherens junction expression between LECs by staining the treated vessels with anti-VE-cadherin antibodies **(Figs. 5A-C)**. Since we introduced fluid directly into the vessel lumen, the degree of junctional disruptions causes "fluid leakage" which is another form of lymphatic dysfunction in addition to impaired lymphatic drainage. Thus, we analyzed endothelial junction disruption by quantifying the junction discontinuities per cell for each treatment condition. While acute inflammation on the order of 2 hours resulted in a modest but not statistically significant increase in junctional disruptions compared to control, chronic inflammation on the order of 48 hours resulted in the statistically significantly higher appearance of junctional disruptions as high as 2.6 times compared to control (*p = 0.0248) **(Fig. 5D)**. This was also accompanied by statistically significantly higher actin signal (**p = 0.0049, control vs. 48 hrs) **(Fig. 5E)** and vessel gap area (*p = 0.0244, control vs. 48 hrs) **(Fig. 5F)** within the vessel as well as lower relative junctional area (*p = 0.0209) **(Fig. 5G)** compared to control. Additionally, live/dead staining of LECs cultured in 3D vessels as in our model showed an increase in cell death (*p = 0.0111) under chronic (48 hrs) inflammation, which was interestingly not seen to the same extent in 2D culture **(Supplementary Fig. 3)**. Collectively, chronic inflammation does not impact lymphatic drainage via compensation of fibrillin expression but leads to a disruption of lymphatic endothelial cell-cell junctions and increases lymphatic permeability and leakage, which is another phenotype of lymphatic dysfunction.

Impaired lymphatic drainage under acute inflammation is attenuated by dexamethasone-mediated restoration of fibrillin expression

In order to reverse the impaired lymphatic drainage under acute inflammation, believed to be mediated by loss of fibrillin, and increased lymphatic permeability under chronic

inflammation, believed to be mediated by the cell junctional disruptions, the microfluidic chips were then subject to the same TNF-α exposure, but pre-treated one day prior with 1 μM of anti-inflammatory dexamethasone. Dexamethasone is an anti-inflammatory glucocorticoid that has previously been shown to promote button-like junction formation between LECs by reversing junctional zippering by *Mycoplasma pulmonis* infection of the respiratory tract in airway lymphatics, hence its use in this study to restore lymphatic drainage and permeability.[22, 41] Lymphatic vessels pre-treated with dexamethasone approximately doubled lymphatic drainage capacity compared to untreated vessels under acute inflammation ($p = 0.0087$) and restored drainage comparable to control levels **(Fig. 6A)**. This was similarly accompanied by 44.7% ($p = 0.0396$) increases in fibrillin area fraction compared to untreated vessels under acute inflammation due to dexamethasone pre-treatment, respectively **(Fig. 6B)**. This is further reflected in immunofluorescent staining of the vessels, where pre-treatment with dexamethasone restored fibrillin density to control levels **(Fig. 6C)**. Thus, the anti-inflammatory effects of dexamethasone reversed the inflammation-induced fibrillin degradation of acute inflammation. However, pre-treatment with dexamethasone only mildly reduced lymphatic permeability compared to untreated vessels under chronic inflammation by 4.28%, respectively, but was not statistically significant **(Fig. 6D)**. This was paralleled by a small reduction of 24.7%, respectively, in vessel gap area **(Fig. 6E)**. Visual representation of this is seen through immunofluorescent staining **(Fig. 6F)**. Taken together, impaired lymphatic drainage under acute inflammation is reversed by dexamethasone, which is correlated with normalization of fibrillin expression. However lymphatic junctional disruption under the chronic inflammation condition was not reserved by the dexamethasone treatment.

Discussion

Though previous *in vitro* studies have examined lymphatic vessel (LV) sprouting,[26, 42-45] LV network formation,[46-48] LV junction/permeability,[31, 49-51] and LV interactions with cancer cells,[52-56] and immune cells.[57-59], there has been no *in vitro* model for studying primary lymphatic valve function. In order to elucidate the mechanisms of primary lymph valve function in the initial lymphatics under normal and inflammation conditions, we created 3D lymphatic vessel (LV) chip devices and examined the effects of TNF-α on lymphatic drainage and permeability, which are regulated by the fluid transport system of the primary lymphatic valves **(Fig. 1)**. From the study, we revealed that acute inflammation reduced anchoring filaments and decreased lymphatic drainage significantly as compared to normal condition when there was high interstitial fluid pressure (expansion phase). The acute inflammation condition, however, made no significant change in lymphatic permeability by forming continuous lymphatic junctions when there was high luminal fluid pressure (compression phase). By contrast, chronic inflammation condition resulted in no significant change in lymphatic drainage when there was high interstitial fluid pressure (expansion phase) by depositing fibrillin. However, chronic inflammation increases lymphatic permeability by causing lymphatic junction disruption and cell death when there is high luminal fluid pressure (compression phase) **(Figs. 2-5)**. Finally, decreased lymphatic drainage under acute inflammation was completely reversed by anti-inflammatory (dexamethasone) treatment with normalization of fibrillin expression **(Fig. 6)**. However lymphatic junctional disruption under the chronic inflammation condition was not reserved by the dexamethasone treatment **(Fig. 6)**.

A possible explanation for the impaired drainage under acute inflammation, the anchoring filaments start to degrade, hence the decrease in the ability of primary valves to open properly for drainage under high interstitial fluid pressure, compared to the normal condition **(Figs. 7A, B)**. By contrast, under chronic inflammation, fibrillin expression and drainage were not affected by fibrillin deposition, but the loss of junctional integrity between lymphatic endothelial cells (LECs) produced a higher permeability of LVs via fluid leakage **(Fig. 7C)**. This is further corroborated by confocal fluorescence imaging of TNF-treated vessels, where VE-cadherin staining of adherens junctions confirms the presence of greater junctional damage and vessel gap area compared with non-treated control **(Fig. 5)**. Therefore, as opposed to acute inflammation, the cause for increased permeability under chronic inflammation appears to induce lymphatic dysfunction **(Fig. 7C)**. In the summary table, the loss of drainage capability under acute inflammation is mostly mediated by the loss of fibrillin and is thus rescued by anti-inflammatory dexamethasone restoration of fibrillin expression, while the increase in permeability under chronic inflammation is mostly mediated by disrupted cell-cell junctions, which was not reversed by dexamethasone **(Fig. 7D)**.

The increase in permeability under chronic inflammation was not attenuated by dexamethasone but was associated with increased actin intensity, disrupted cell-cell junctions **(Fig. 5)**, and potential LEC deaths **(Supplementary Fig. 3)**. Previously, several studies reported that the chronic inflammation condition involves cell deaths.[60-62] Also, TNF-α has been shown to reduce the proliferation of lymphatic endothelial cells (LECs) at concentrations as low as 5 ng/mL.[63] Another previous study demonstrated TNF-α stimulation of primary dermal LECs *in vitro* increasing the presence of discontinuous junction and reducing the broad distribution of VE-cadherin at the cell periphery, accompanied by endothelial cell elongation in parallel with a high density of actin stress fibers and reduction in cell-cell overlapping areas as cells separate from apoptosis.[64] For LECs, the connections between adherens junctions and actin filaments are mediated by VE-cadherin and are believed to be crucial for endothelial remodeling, including cellular reactions to various endothelial permeability factors.[65] Thus, increased actin fiber signal and vessel gap area **(Fig. 5)** may be indicative of junctional remodeling and discontinuous junction formation. Given that discontinuities between LECs allow for potential leakage into the interstitium, these results align with the finding that chronic inflammation witnesses increased lymphatic permeability.

Though we have focused on lymphatic drainage and permeability in separate experiments, the idea that lymphatic

dysfunction relies on fibrillin and the resultant drainage should also be more examined in conjunction with the presence of VE-cadherin and junctional components. This is especially relevant given the emerging view that LEC junctional remodeling plays a role in disease pathogenesis, affecting RhoA/ROCK activity or endothelial-to-mesenchymal transition.[25, 66, 67] Past studies have already identified transmembrane integrins, vinculin, talin, focal adhesion kinase (FAK), and Emilin-1 as essential molecules in assisting the anchoring filament connection between the extracellular matrix and endothelial cell cytoskeleton, providing potential targets for future analysis.[68]

Additionally, the nanospheres utilized were drained into the LEC channel over the course of 16 hours, which we have found through past studies to be the optimum time for fluid equilibrium to occur across the microfluidic chip in similar systems.[30] Imaging nanosphere migration would require 16 hours of live microscopy imaging, which cannot be guaranteed to preserve the same conditions (CO_2 and humidity) of cell incubators and cannot provide luminal flow along the vessel axis that is required for proper LEC phenotype and vessel formation *in vitro*.[48] Thus, the data presented here represents the total drainage of nanospheres after equilibrium is reached, measured using the fluorescence intensity of nanospheres accumulated on each side of the chip. More complex live microscopy techniques that allow for control of luminal flow and longer time periods of imaging would be needed to explore this in future studies.

Indeed, lymphatic junction remodelling in inflammation has been assessed *in vitro* and *in vivo*; however, it has raised some controversies. Previous *in vitro* studies have demonstrated that inflammatory cytokine stimulation impairs LEC barrier function and increases diffusive permeability in 2D LEC culture via the reduced expression of VE-cadherin.[37] However, several other *in vivo* studies have found that inflammation transforms LEC button-like junctions into less permeable zipper-like junctions. Especially, the zipper-like junctions were predominant in new LVs formed by inflammation-associated lymphangiogenesis.[69, 70] This follows with the finding that junctional zippering produces less permeable LVs that reduce fluid entry and clearance, aggravating lymphedema normally found in inflammatory diseases, and is supported by observations of decreased lymph flow under chronic inflammation.[71-73] This is also related to viral infections that can zipper lymphatic junctions to stop further dissemination of the viruses within the host.[74] Consistently, our previous study using 3D lymphatics-on-chip models showed fibronectin, a major component of inflammation-associated ECM, zippered LEC junction via activating integrin alpha 5 in LECs.[31] Similarly, in this study, our acute inflammation via TNF-α occurred over the course of 2 hours, and we found the lymphatic drainage was reduced via relatively intact LEC junctions and reduced anchoring filaments. However, in our chronic inflammation via TNF-α treatments over the course of 48 hours, we saw junction disruption and increased permeability. Other studies suggest that increased lymph flow and fluid drainage are observed at the onset of inflammation in diseases such as rheumatoid arthritis.[72, 75] Given the controversial outcomes in chronic or acute inflammation *in vitro* and *in vivo*, it is required to precisely model the conditions with appropriate cytokines with the proper dosages and durations. Our model used a practical mimic of chronic inflammation that occurs in inflammatory and autoimmune conditions rather than on the order of several days or weeks that are possible with the aforementioned *in vivo* studies, so it is guaranteed for further investigation in the longer-term exposures with inflammatory cytokines.

There are some limitations in the current model system. Regarding permeability through the button junctions, past studies have shown that the solute permeability for lymphatic capillaries *in vivo* was 14×10^{-7} cm/s [76], while permeability of engineered LEC tubes from other *in vitro* models to bovine serum albumin and 10 kDa dextran was 1.4×10^{-6} cm/s and 1.7×10^{-6} cm/s, respectively.[77] Our data similarly suggest that *in vitro* models of LVs are far more permeable than their *in vivo* counterparts, which may result from the lack of complete stromal cells as well as the larger lumen size in comparison to bodily lymphatics and higher luminal fluid pressure than *in vivo* conditions. The inclusion of parenchymal or stromal cells and immune cells within this model could provide a more biomimetic representation of physiologically relevant autoimmune diseases. Additionally, our model simulated luminal flow by oscillatory rocking, but more advanced *in vitro* models would mimic the multicellularity, architecture, and flow conditions of native vessels. Moreover, throughout the study, TNF-α was used as the main component of the inflammatory microenvironment, given that TNF-α activity is implicated in inflammatory diseases such as autoimmune diseases.[78, 79] However, other cytokines can be involved and contribute to primary valve dysfunction, which can perhaps be verified with *in vivo* models. Lastly, there is a limitation of the study regarding that we could not visualize and characterize the anchoring filaments' interactions with cells and extracellular matrix.

Conclusions

Our study provides some of the first examinations of primary lymphatic valve function using an *in vitro* microfluidic chip model, demonstrating impaired lymphatic drainage and permeability under inflammation due to the degradation of anchoring filaments and related lymphatic junction disruption. Regarding the relative contributions of acute or chronic inflammation to the primary lymph valve dysfunction, acute inflammation mainly impaired lymphatic drainage, but chronic inflammation impaired permeability, potentially exacerbating the dysfunction. This primary lymph valve chip may provide a unique platform for furthering our understanding and rendering feasible high-throughput testing of drug candidates in the lymphatic microenvironment.

Author Contributions

Samantha Kraus (S.K.): conceptualization, investigation, methodology, visualization, and writing – original draft.
Esak Lee (E.L.): conceptualization, funding acquisition, project administration, supervision, discussion, and writing – review & editing.

Conflicts of interest

There are no conflicts to declare. This manuscript is approved by all authors for publication.

Acknowledgments

We thank Renhao Lu for the design of the microfluidic chip and Young Kwon Hong of the University of Southern California for supplying primary human dermal microvascular lymphatic endothelial cells. The authors (S.E.K., E.L.) would like to thank the NIH grants (AI166772, AI168886, HL165135, CA279560). S.E.K. was supported by the NSF Graduate Research Fellowships Program (NSF GRFP) and the Cornell Presidential Life Science Fellowship (PLSF). This work was performed in part at the Cornell NanoScale Facility (CNF), a member of the National Nanotechnology Coordinated Infrastructure (NNCI), which is supported by the National Science Foundation (Grant NNCI-2025233).

References

1. T. V. Petrova and G. Y. Koh, *Science*, 2020, **369**.
2. P. Baluk, J. Fuxe, H. Hashizume, T. Romano, E. Lashnits, S. Butz, D. Vestweber, M. Corada, C. Molendini, E. Dejana and D. M. McDonald, *J Exp Med*, 2007, **204**, 2349-2362.
3. S. Chakraborty, M. J. Davis and M. Muthuchamy, *Seminars in Cell & Developmental Biology*, 2015, **38**, 55-66.
4. A. Aspelund, M. R. Robciuc, S. Karaman, T. Makinen and K. Alitalo, *Circulation Research*, 2016, **118**, 515-530.
5. W. Wang, Z. Nepiyushchikh, D. C. Zawieja, S. Chakraborty, S. D. Zawieja, A. A. Gashev, M. J. Davis and M. Muthuchamy, *Am J Physiol Heart Circ Physiol*, 2009, **297**, H726-734.
6. M. Muthuchamy, A. Gashev, N. Boswell, N. Dawson and D. Zawieja, *FASEB J*, 2003, **17**, 920-922.
7. J. T. Wilson, R. van Loon, W. Wang, D. C. Zawieja and J. E. Moore, Jr., *J Biomech*, 2015, **48**, 3584-3590.
8. K. Nonomura, V. Lukacs, D. T. Sweet, L. M. Goddard, A. Kanie, T. Whitwam, S. S. Ranade, T. Fujimori, M. L. Kahn and A. Patapoutian, *P Natl Acad Sci USA*, 2018, **115**, 12817-12822.
9. E. Bazigou, S. Xie, C. Chen, A. Weston, N. Miura, L. Sorokin, R. Adams, A. F. Muro, D. Sheppard and T. Makinen, *Developmental Cell*, 2009, **17**, 175-186.
10. T. Kume, *J Clin Invest*, 2015, **125**, 2924-2926.
11. Y. Yang, B. Cha, Z. Y. Motawe, R. S. Srinivasan and J. P. Scallan, *Cell Reports*, 2019, **28**, 2397-+.
12. S. Schulte-Merker, A. Sabine and T. V. Petrova, *J Cell Biol*, 2011, **193**, 607-618.
13. J. Trzewik, S. K. Mallipattu, G. M. Artmann, F. A. Delano and G. W. Schmid-Schönbein, *FASEB J*, 2001, **15**, 1711-1717.
14. G. W. Schmid-Schönbein, *Lymphat Res Biol*, 2003, **1**, 25-29; discussion 29-31.
15. L. V. Leak and J. F. Burke, *J Cell Biol*, 1968, **36**, 129-149.
16. E. Bazigou, J. T. Wilson and J. E. Moore, *Microvasc Res*, 2014, **96**, 38-45.
17. E. Mendoza and G. W. Schmid-Schönbein, *J Biomech Eng*, 2003, **125**, 407-414.
18. C. Danussi, P. Spessotto, A. Petrucco, B. Wassermann, P. Sabatelli, M. Montesi, R. Doliana, G. M. Bressan and A. Colombatti, *Mol Cell Biol*, 2008, **28**, 4026-4039.
19. C. Danussi, L. Del Bel Belluz, E. Pivetta, T. M. Modica, A. Muro, B. Wassermann, R. Doliana, P. Sabatelli, A. Colombatti and P. Spessotto, *Mol Cell Biol*, 2013, **33**, 4381-4394.
20. S. Liao and P. Y. von der Weid, *Angiogenesis*, 2014, **17**, 325-334.
21. N. Schwartz, M. L. S. Chalasani, T. M. Li, Z. Feng, W. D. Shipman and T. T. Lu, *Front Immunol*, 2019, **10**, 519.
22. L. C. Yao, P. Baluk, R. S. Srinivasan, G. Oliver and D. M. McDonald, *Am J Pathol*, 2012, **180**, 2561-2575.
23. R. S. Czepielewski, E. C. Erlich, E. J. Onufer, S. Young, B. T. Saunders, Y. H. Han, M. Wohltmann, P. L. Wang, K. W. Kim, S. Kumar, C. S. Hsieh, J. P. Scallan, Y. Yang, B. H. Zinselmeyer, M. J. Davis and G. J. Randolph, *Immunity*, 2021, **54**, 2795-2811.e2799.
24. P. M. Lynch, F. A. Delano and G. W. Schmid-Schönbein, *Lymphat Res Biol*, 2007, **5**, 3-10.
25. F. Zhang, G. Zarkada, J. Han, J. Li, A. Dubrac, R. Ola, G. Genet, K. Boyé, P. Michon, S. E. Künzel, J. P. Camporez, A. K. Singh, G. H. Fong, M. Simons, P. Tso, C. Fernández-Hernando, G. I. Shulman, W. C. Sessa and A. Eichmann, *Science*, 2018, **361**, 599-603.
26. D. Choi, E. Park, E. Jung, Y. J. Seong, J. Yoo, E. Lee, M. Hong, S. Lee, H. Ishida, J. Burford, J. Peti-Peterdi, R. H. Adams, S. Srikanth, Y. Gwack, C. S. Chen, H. J. Vogel, C. J. Koh, A. K. Wong and Y. K. Hong, *J Clin Invest*, 2017, **127**, 1225-1240.
27. D. Choi, E. Park, E. Jung, Y. J. Seong, M. Hong, S. Lee, J. Burford, G. Gyarmati, J. Peti-Peterdi, S. Srikanth, Y. Gwack, C. J. Koh, E. Boriushkin, A. Hamik, A. K. Wong and Y. K. Hong, *Circ Res*, 2017, **120**, 1426-1439.
28. T. J. Kwak and E. Lee, *Biofabrication*, 2020, **13**.
29. T. J. Kwak and E. Lee, *Sci Rep*, 2020, **10**, 20142.
30. P. A. Soden, A. R. Henderson and E. Lee, *Adv Biol (Weinh)*, 2022, DOI: 10.1002/adbi.202200027, e2200027.
31. A. R. Henderson, I. S. Ilan and E. Lee, *Microcirculation*, 2021, **28**, e12730.
32. V. W. Tang, *Mol Biol Cell*, 2020, **31**, 1823-1834.
33. A. A. Tomei, S. Siegert, M. R. Britschgi, S. A. Luther and M. A. Swartz, *J Immunol*, 2009, **183**, 4273-4283.
34. C. Valero, H. Amaveda, M. Mora and J. M. García-Aznar, *PLoS One*, 2018, **13**, e0195820.
35. S. Pérez-Rodríguez, S. A. Huang, C. Borau, J. M. García-Aznar and W. J. Polacheck, *Biomicrofluidics*, 2021, **15**, 054102.
36. J. B. Dixon, S. T. Greiner, A. A. Gashev, G. L. Cote, J. E. Moore and D. C. Zawieja, *Microcirculation*, 2006, **13**, 597-610.
37. W. E. Cromer, S. D. Zawieja, B. Tharakan, E. W. Childs, M. K. Newell and D. C. Zawieja, *Angiogenesis*, 2014, **17**, 395-406.
38. W. J. Polacheck, M. L. Kutys, J. Yang, J. Eyckmans, Y. Wu, H. Vasavada, K. K. Hirschi and C. S. Chen, *Nature*, 2017, **552**, 258-262.
39. J. Schindelin, I. Arganda-Carreras, E. Frise, V. Kaynig, M. Longair, T. Pietzsch, S. Preibisch, C. Rueden, S. Saalfeld, B. Schmid, J. Y. Tinevez, D. J. White, V. Hartenstein, K. Eliceiri,

P. Tomancak and A. Cardona, *Nat Methods*, 2012, **9**, 676-682.
40. C. A. Schneider, W. S. Rasband and K. W. Eliceiri, *Nat Methods*, 2012, **9**, 671-675.
41. L. C. Yao, P. Baluk, J. Feng and D. M. McDonald, *Am J Pathol*, 2010, **176**, 1525-1541.
42. S. Kim, M. Chung and N. L. Jeon, *Biomaterials*, 2016, **78**, 115-128.
43. T. Osaki, J. C. Serrano and R. D. Kamm, *Regen Eng Transl Med*, 2018, **4**, 120-132.
44. F. Bruyere, L. Melen-Lamalle, S. Blacher, G. Roland, M. Thiry, L. Moons, F. Frankenne, P. Carmeliet, K. Alitalo, C. Libert, J. P. Sleeman, J. M. Foidart and A. Noel, *Nat Methods*, 2008, **5**, 431-437.
45. S. Kumaravel, C. A. Abbey, K. J. Bayless and S. Chakraborty, *Am J Physiol Cell Physiol*, 2020, **319**, C1045-C1058.
46. L. Gibot, T. Galbraith, J. Bourland, A. Rogic, M. Skobe and F. A. Auger, *Nat Protoc*, 2017, **12**, 1077-1088.
47. L. Gibot, T. Galbraith, B. Kloos, S. Das, D. A. Lacroix, F. A. Auger and M. Skobe, *Biomaterials*, 2016, **78**, 129-139.
48. A. Rogic, F. Auger and M. Skobe, *Methods Mol Biol*, 2018, **1846**, 279-290.
49. J. M. Ayuso, M. M. Gong, M. C. Skala, P. M. Harari and D. J. Beebe, *Adv Healthc Mater*, 2020, **9**, e1900925.
50. M. M. Gong, K. M. Lugo-Cintron, B. R. White, S. C. Kerr, P. M. Harari and D. J. Beebe, *Biomaterials*, 2019, **214**.
51. I. S. Ilan, A. R. Yslas, Y. Peng, R. Lu and E. Lee, *Cell Mol Bioeng*, 2023, DOI: https://doi.org/10.1007/s12195-023-00780-0.
52. K. M. Lugo-Cintron, J. M. Ayuso, B. R. White, P. M. Harari, S. M. Ponik, D. J. Beebe, M. M. Gong and M. Virumbrales-Munoz, *Lab Chip*, 2020, **20**, 1586-1600.
53. N. Frenkel, S. Poghosyan, C. R. Alarcon, S. B. Garcia, K. Queiroz, L. van den Bent, J. Laoukili, I. B. Rinkes, P. Vulto, O. Kranenburg and J. Hagendoorn, *ACS Biomater Sci Eng*, 2021, **7**, 3030-3042.
54. X. Cao, R. Ashfaq, F. Cheng, S. Maharjan, J. Li, G. Ying, S. Hassan, H. Xiao, K. Yue and Y. S. Zhang, *Adv Funct Mater*, 2019, **29**.
55. J. Bourland, J. Fradette and F. A. Auger, *Sci Rep*, 2018, **8**, 13191.
56. M. Pisano, V. Triacca, K. A. Barbee and M. A. Swartz, *Integr Biol (Camb)*, 2015, **7**, 525-533.
57. K. G. Birmingham, M. J. O'Melia, S. Bordy, D. Reyes Aguilar, B. El-Reyas, G. Lesinski and S. N. Thomas, *iScience*, 2020, **23**, 101751.
58. T. Kraus, A. Lubitz, U. Schliesser, C. Giese, J. Reuschel, R. Brecht, J. Engert and G. Winter, *J Pharm Sci*, 2019, **108**, 2358-2366.
59. J. H. Hammel, S. R. Cook, M. C. Belanger, J. M. Munson and R. R. Pompano, *Annu Rev Biomed Eng*, 2021, **23**, 461-491.
60. J. V. Patankar and C. Becker, *Nat Rev Gastroenterol Hepatol*, 2020, **17**, 543-556.
61. H. Anderton, I. P. Wicks and J. Silke, *Nat Rev Rheumatol*, 2020, **16**, 496-513.
62. Y. Yu, Y. Yan, F. Niu, Y. Wang, X. Chen, G. Su, Y. Liu, X. Zhao, L. Qian, P. Liu and Y. Xiong, *Cell Death Discov*, 2021, **7**, 193.
63. G. V. Chaitanya, S. E. Franks, W. Cromer, S. R. Wells, M. Bienkowska, M. H. Jennings, A. Ruddell, T. Ando, Y. Wang, Y. Gu, M. Sapp, J. M. Mathis, P. A. Jordan, A. Minagar and J. S. Alexander, *Lymphat Res Biol*, 2010, **8**, 155-164.
64. Y. Kakei, M. Akashi, T. Shigeta, T. Hasegawa and T. Komori, *Lymphat Res Biol*, 2014, **12**, 136-143.
65. E. Dejana, F. Orsenigo and M. G. Lampugnani, *J Cell Sci*, 2008, **121**, 2115-2122.
66. T. Ichise, N. Yoshida and H. Ichise, *J Cell Sci*, 2014, **127**, 845-857.
67. Y. Yoshimatsu, S. Kimuro, J. Pauty, K. Takagaki, S. Nomiyama, A. Inagawa, K. Maeda, K. A. Podyma-Inoue, K. Kajiya, Y. T. Matsunaga and T. Watabe, *PLoS One*, 2020, **15**, e0232356.
68. R. Gerli, R. Solito, E. Weber and M. Aglianó, *Lymphology*, 2000, **33**, 148-157.
69. L. C. Yao, C. Testini, D. Tvorogov, A. Anisimov, S. O. Vargas, P. Baluk, B. Pytowski, L. Claesson-Welsh, K. Alitalo and D. M. McDonald, *Circ Res*, 2014, **114**, 806-822.
70. H. Kim, R. P. Kataru and G. Y. Koh, *J Clin Invest*, 2014, **124**, 936-942.
71. R. Huggenberger, S. Ullmann, S. T. Proulx, B. Pytowski, K. Alitalo and M. Detmar, *J Exp Med*, 2010, **207**, 2255-2269.
72. Q. Zhou, R. Wood, E. M. Schwarz, Y.-J. Wang and L. Xing, *Arthritis & Rheumatism*, 2010, DOI: 10.1002/art.27464, NA-NA.
73. W. Cromer, W. Wang, S. D. Zawieja, P. Y. von der Weid, M. K. Newell-Rogers and D. C. Zawieja, *Inflamm Bowel Dis*, 2015, **21**, 1553-1563.
74. M. J. Churchill, H. du Bois, T. A. Heim, T. Mudianto, M. M. Steele, J. C. Nolz and A. W. Lund, *J Exp Med*, 2022, **219**.
75. J. N. Benoit, D. C. Zawieja, A. H. Goodman and H. J. Granger, *Am J Physiol*, 1989, **257**, H2059-2069.
76. J. P. Scallan and V. H. Huxley, *J Physiol*, 2010, **588**, 243-254.
77. G. M. Price, K. M. Chrobak and J. Tien, *Microvasc Res*, 2008, **76**, 46-51.
78. P. Li, Y. Zheng and X. Chen, *Front Pharmacol*, 2017, **8**, 460.
79. M. Komatsu, D. Kobayashi, K. Saito, D. Furuya, A. Yagihashi, H. Araake, N. Tsuji, S. Sakamaki, Y. Niitsu and N. Watanabe, *Clin Chem*, 2001, **47**, 1297-1301.

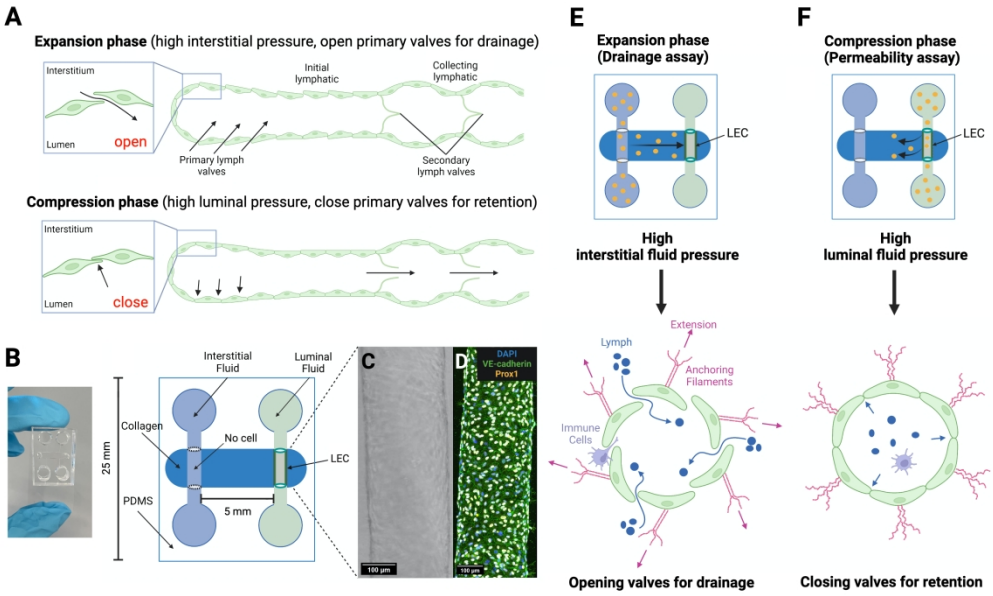

Figure 1. An engineered 3D lymphatic vessel model to examine primary lymphatic valve function in vitro. (A) A representation of primary and secondary lymph valves in initial and collecting lymphatic vessels, respectively, in vivo. During the expansion phase, greater hydrostatic pressure in the interstitium surrounding the initial lymphatic vessel causes microvalves to open and fluid to enter (top). During the compression phase, greater pressure in the vessel lumen closes the microvalves and opens the secondary lymph valves, causing fluid to flow downstream (bottom). (B) A schematic of the organotypic 3D lymphatic vessel model (lymphatic vessel-on-chip), with a channel of lymphatic endothelial cells (LECs) embedded in collagen 1 matrix and an acellular channel to induce interstitial fluid flow. (C) A representative bright-field image of engineered rudimentary lymphatic vessels. (D) An engineered lymphatic vessel stained with anti-Prox1 (a lymphatic endothelial marker) antibodies, anti-VE-cadherin (adherens junctions) antibodies, and DAPI (cell nuclei) to show LEC identification. (E, F) Two settings of experiments to represent primary lymphatic valve function in the initial lymphatic vessels. (E) Upon increase in interstitial fluid pressure, anchoring filaments pull the overlapping junctions apart and allow entry of fluid and immune cells towards the lumen, which can be modeled in vitro by introducing interstitial fluid to the acellular channel (left-side channel) and measuring fluid drainage into the lymphatic vessel (drainage assay). (F) After the initial fluid drainage, the luminal fluid pressure becomes higher than the interstitial fluid pressure. In this condition, primary lymphatic valves close the overlapping junctions and keep the lymph and molecules or immune cells within the lumen, which can be modeled by introducing lymph fluid directly to the lumen of the engineered lymphatic vessel (right-side channel) and measuring diffusion of the fluid to the interstitial space (permeability assay).

728x433mm (118 x 118 DPI)

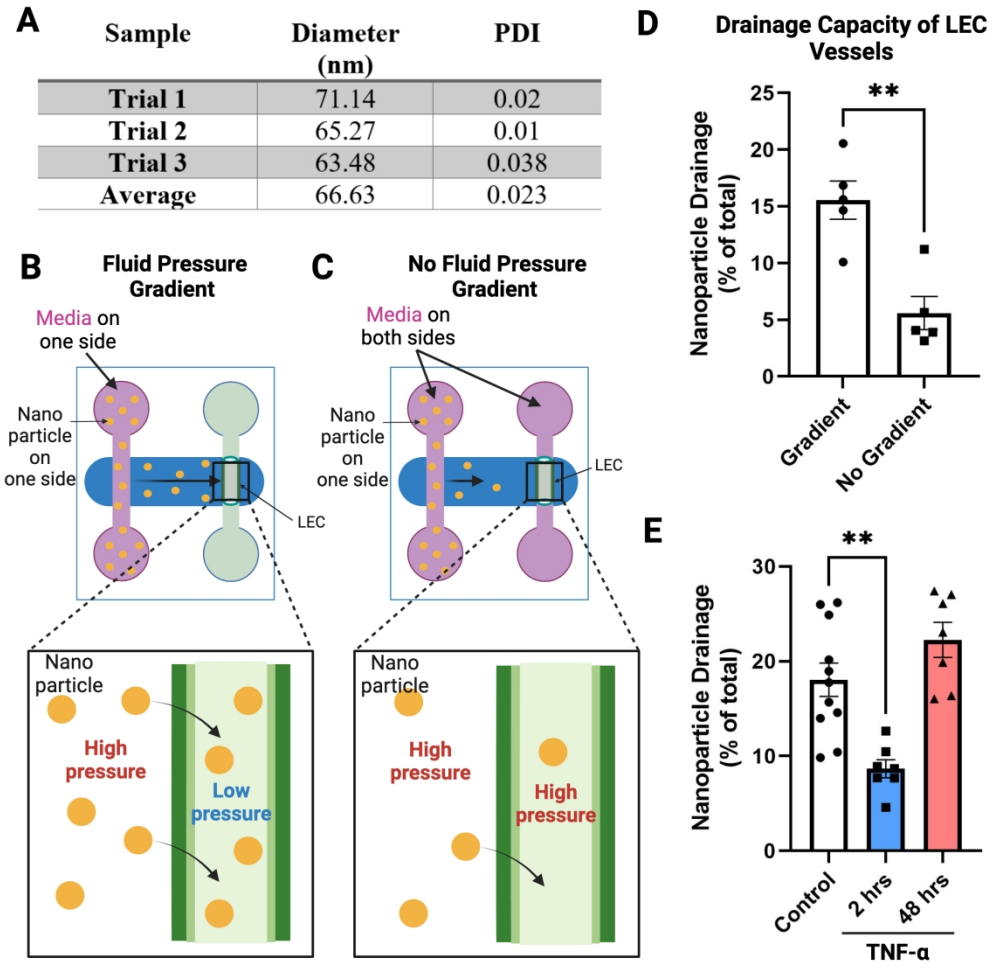

Figure 2. Effects of acute and chronic inflammation on lymphatic drainage. (A) Quantification of fluorescent dragon green nanosphere diameter by dynamic light scattering (DLS). Size measurements were collected on a Malvern Nano ZS Zetasizer at 25°C. Data are expressed as mean values. A representation of the drainage assay performed, in which (B) media is added to only one side of the chip in order to create a fluid pressure gradient toward the lymphatic vessel, and in which (C) media is added to both sides of the chip to create equal pressure, eliminating the fluid pressure gradient. In all the cases, nanoparticles were only introduced to one side of the channels. (D) Quantification of lymphatic drainage (% of total) with and without the presence of a fluid pressure gradient for the vessel. Drainage capacity of lymphatic vessels as a percentage of total nanoparticles drained. ** p = 0.0021; Two-tailed unpaired Student t- test, n = 5 per group. Data are expressed as mean ± S.E.M. (E) Quantification of lymphatic drainage (% of total) under acute and chronic inflammation. Drainage capacity of lymphatic vessels as a percentage of total nanoparticles drained across 10-20 ng/mL TNF-α concentration in different exposure times (one-time TNF-α exposure for 2 hours for modeling acute inflammation and repeated TNF-α exposures for 48 hours for modeling chronic inflammation). ** p = 0.0018; One-way ANOVA with Tukey's HSD tests, n shown as individual data points for each group. Data are expressed as mean ± S.E.M.

561x551mm (118 x 118 DPI)

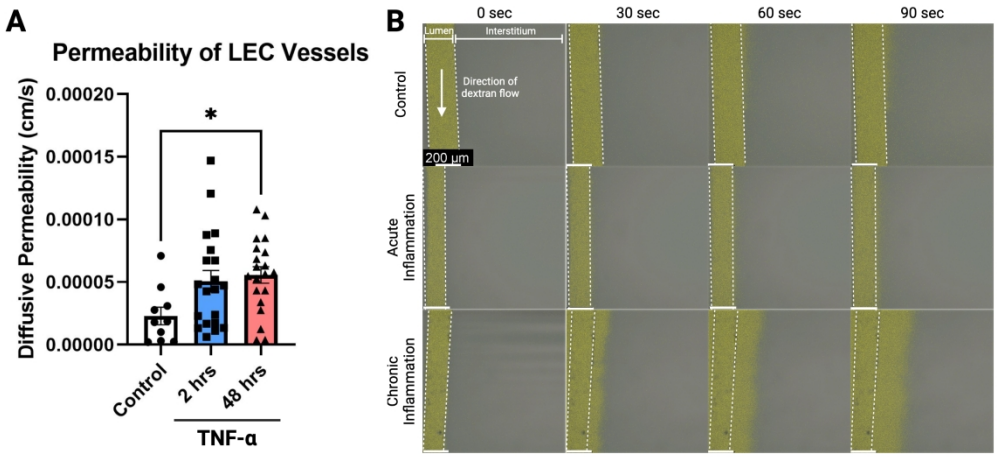

Figure 3. Effects of acute and chronic inflammation on lymphatic permeability. (A) Quantification of lymphatic permeability under acute and chronic inflammation. 70 kDa dextran was introduced into the vessel lumens and dextran diffusion was observed in real-time under microscopy. Diffusive permeability across 10-20 ng/mL TNF-α concentration in different exposure times (2 hours for acute inflammation and 48 hours for chronic inflammation). * p = 0.0319; One-way ANOVA with Tukey's HSD tests, n shown as individual data points for each group. Data are expressed as mean ± S.E.M. (B) Representative images of leakage of 70 kDa dextran out of lymphatic vessels with or without exposure to acute (shown here as vessels treated for 2 hours with 10 ng/mL of TNF-α) or chronic inflammation (shown here as vessels treated for 48 hours with 10 ng/mL of TNF-α several times).

593x274mm (118 x 118 DPI)

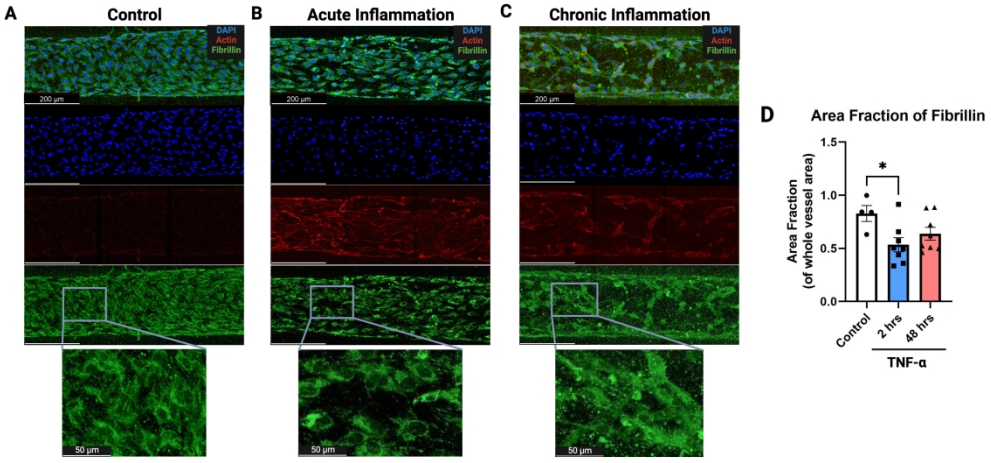

Figure 4. Effects of acute and chronic inflammation on fibrillin, a component of anchoring filaments. (A) Fibrillin, actin (phalloidin), and DAPI staining on control lymphatic vessels with no cytokine treatment. (B) Fibrillin, actin, and DAPI staining on lymphatic vessels under acute inflammation (10-20 ng/mL of TNF-α treatment for 2 hours). (C) Fibrillin, actin, and DAPI staining on lymphatic vessels under chronic inflammation (10-20 ng/mL of TNF-α treatments for 48 hours). (D) Quantification of area fraction of fibrillin signal normalized by the whole vessel area across different concentrations and exposure times of TNF-α. * p = 0.0349; One-way ANOVA with Tukey's HSD tests, n shown as individual data points for each group. Data are expressed as mean ± S.E.M.

710x335mm (118 x 118 DPI)

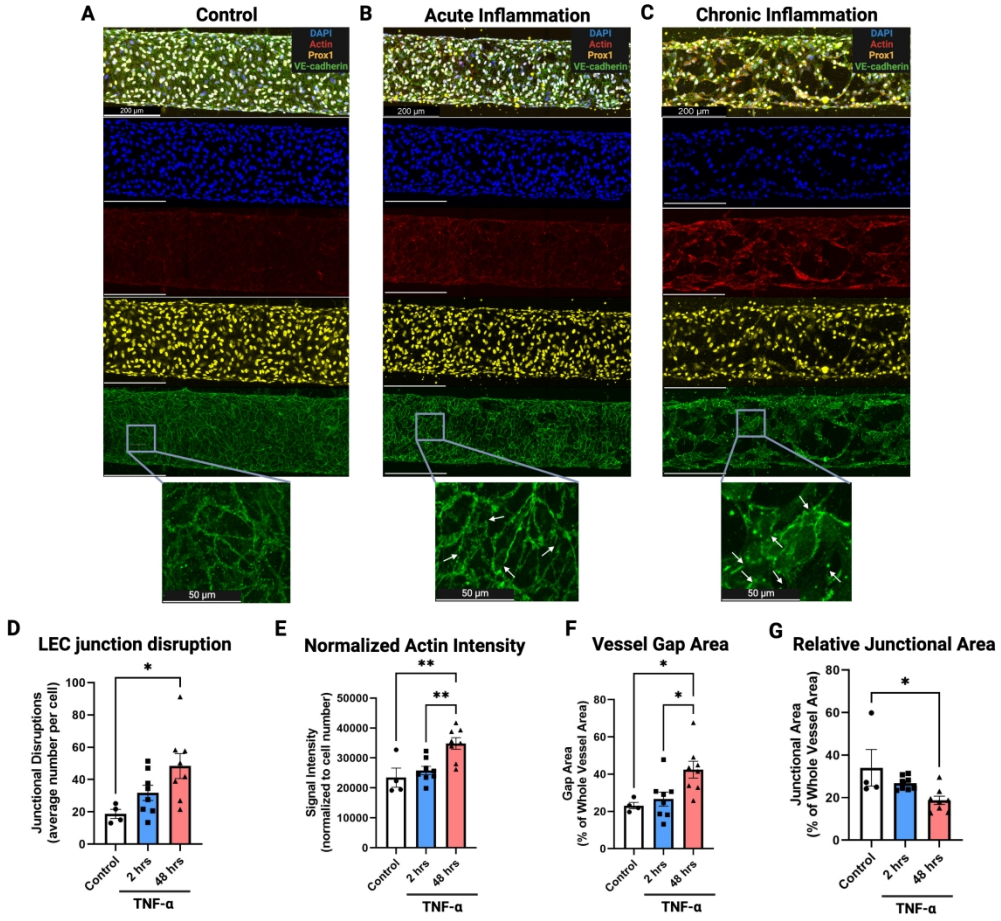

Figure 5. Effects of acute and chronic inflammation on lymphatic junctions. (A) VE-cadherin, Prox1, actin (phalloidin), and DAPI staining on control lymphatic vessels with no cytokine treatment. (B) VE-cadherin, Prox1, actin, and DAPI staining on lymphatic vessels under acute inflammation (10-20 ng/mL of TNF-α treatment for 2 hours). (C) VE-cadherin, Prox1, actin, and DAPI staining on lymphatic vessels under chronic inflammation (10-20 ng/mL of TNF-α treatments for 48 hours). Arrows in the enlarged images indicate the presence of junctional disruptions. (D) Quantification of the average number of disruptions per cell across different concentrations and exposure times of TNF-α. * p = 0.0248. (E) Quantification of the actin signal intensity normalized to cell number across different concentrations and exposure times of TNF-α. ** p = 0.0049 (Control vs. 48 hrs), ** p = 0.0063 (2 hrs vs. 48 hrs); (F) Quantification of the vessel gap area as a percentage of whole vessel area across different concentrations and exposure times of TNF-α. * p = 0.0244 (Control vs. 48 hrs), * p = 0.0239 (2 hrs vs. 48 hrs); (G) Quantification of the relative cell junctional area as a percentage of whole vessel area across different concentration and exposure times of TNF-α. * p = 0.0209; One-way ANOVA with Tukey's HSD tests, n shown as individual data points for each group. Data are expressed as mean ± S.E.M.

628x584mm (118 x 118 DPI)

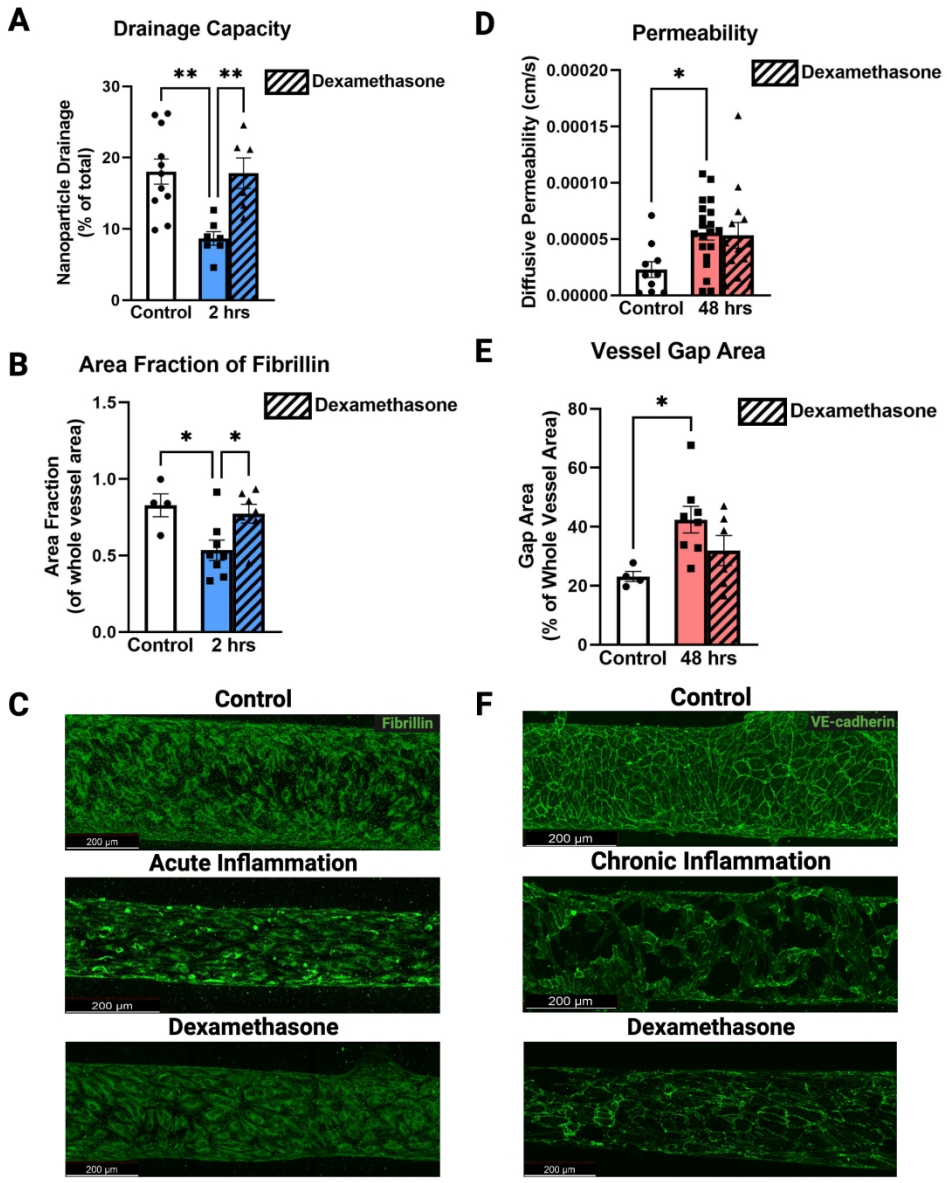

Figure 6. Effects of anti-inflammatory dexamethasone treatment on impaired lymphatic drainage and permeability. (A) Quantification of lymphatic drainage (% of total) under acute inflammation and pre-treatment with dexamethasone. ** p = 0.0022 (Control vs. 2hrs), ** p = 0.0087 (2 hrs vs. 2 hrs + dexamethasone); (B) Quantification of area fraction of fibrillin signal normalized by the whole vessel area under acute inflammation and pre-treatment with dexamethasone. * p = 0.0321 (Control vs. 2 hrs), * p = 0.0396 (2 hrs vs. 2 hrs + dexamethasone); (C) Fibrillin staining on lymphatic vessels under acute inflammation pre-treated with dexamethasone. (D) Quantification of lymphatic permeability under chronic inflammation and pre-treatment with dexamethasone. * p = 0.0316; (E) Quantification of the vessel gap area as a percentage of the whole vessel area under chronic inflammation and pre-treatment with dexamethasone. * p = 0.0368; (F) VE-cadherin staining on lymphatic vessels under chronic inflammation pre-treated with dexamethasone. One-way ANOVA with Tukey's HSD tests, n shown as individual data points for each group. Data are expressed as mean ± S.E.M.

427x531mm (118 x 118 DPI)

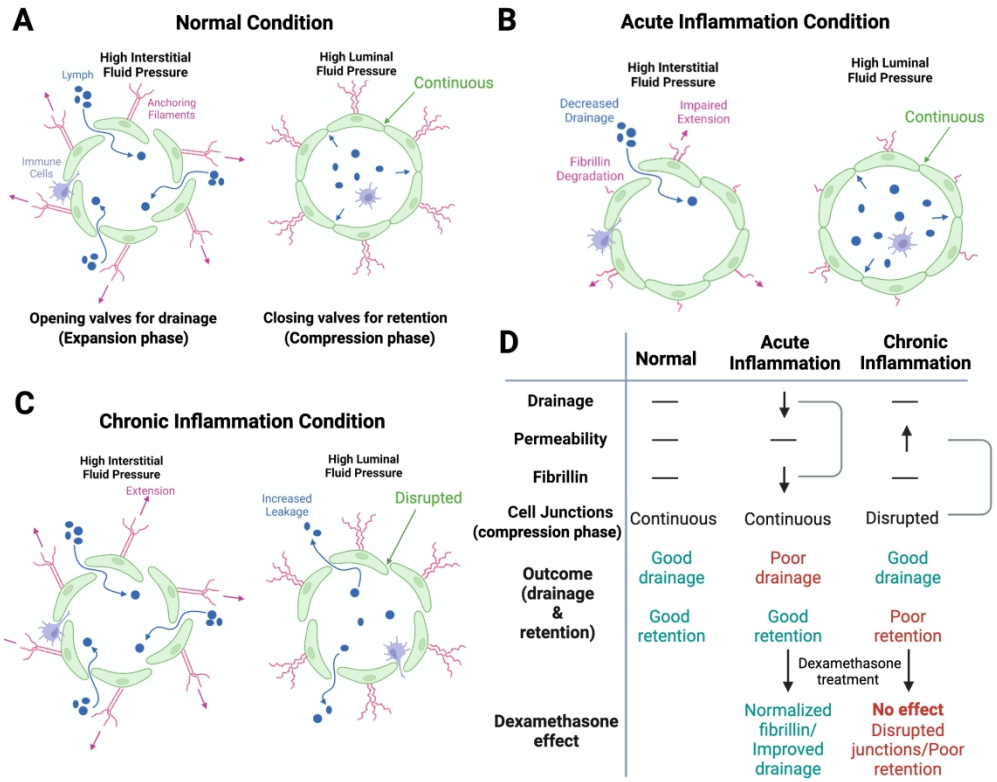

Figure 7. A potential mechanism of dysfunction of primary lymphatic valves in acute and chronic inflammation and the dexamethasone effects against the inflammatory conditions. (A) In normal conditions, lymphatic drainage is maintained at high levels by extension of anchoring filaments, and lymphatic permeability is maintained at low levels by relaxation of anchoring filaments and closing of flap valves. (B) Under acute inflammation, degradation of fibrillin results in impaired extension of anchoring filaments, leading to decreased drainage, and retention of fluid, which is supported by intact lymphatic junctions. (C) Under chronic inflammation, anchoring filament extension occurs via the re-deposited fibrillin leading to normal fluid drainage, but increased permeability of fluid from leakage, which is due to increased junction discontinuities. (D) In summary, loss of drainage capability under acute inflammation is mostly mediated by loss of fibrillin, which can be reversed by dexamethasone treatment. The increase in permeability under chronic inflammation is mostly mediated by disrupted cell junctions, which cannot be reversed by dexamethasone treatment.

626x489mm (118 x 118 DPI)